Average and local structure, Debye temperature, and structural rigidity in some oxide compounds related to phosphor hosts

Kristin A. Denault,[†,‡] Jakoah Brgoch,[¶] Simon D. Kloß,[†,§] Michael W. Gaultois,[†,‖] Joan Siewenie,[⊥] Katharine Page,[⊥,#] and Ram Seshadri[*,†,‡,‖]

Materials Research Laboratory, University of California, Santa Barbara, CA 93106, Materials Department, University of California, Santa Barbara, CA 93106, Department of Chemistry, University of Houston, Houston, TX 77024, Department Chemie, Ludwig-Maximilians-Universität, Munich, DE 81377, Germany, Department of Chemistry and Biochemistry, University of California, Santa Barbara, CA 93106, Lujan Neutron Scattering Center, Los Alamos National Laboratory, NM 87545, and Spallation Neutron Source, Oak Ridge National Lab, Oak Ridge, TN 37831-6475

E-mail: seshadri@mrl.ucsb.edu

---

[*]To whom correspondence should be addressed
[†]Materials Research Laboratory, University of California, Santa Barbara, CA 93106
[‡]Materials Department, University of California, Santa Barbara, CA 93106
[¶]Department of Chemistry, University of Houston, Houston, TX 77024
[§]Department Chemie, Ludwig-Maximilians-Universität, Munich, DE 81377, Germany
[‖]Department of Chemistry and Biochemistry, University of California, Santa Barbara, CA 93106
[⊥]Lujan Neutron Scattering Center, Los Alamos National Laboratory, NM 87545
[#]Spallation Neutron Source, Oak Ridge National Lab, Oak Ridge, TN 37831-6475

Abstract

The average and local structure of the oxides Ba_2SiO_4, $BaAl_2O_2$, $SrAl_2O_4$, and Y_2SiO_5 are examined in order to evaluate crystal rigidity in light of recent studies suggesting that highly connected and rigid structures yield the best phosphor hosts. Simultaneous momentum-space refinements of synchrotron X-ray and neutron scattering yield accurate average crystal structures, with reliable atomic displacement parameters. The Debye temperature Θ_D, which has proven to be a useful proxy for structural rigidity, is extracted from the experimental atomic displacement parameters and compared with predictions from density functional theory calculations and experimental low-temperature heat capacity measurements. The role of static disorder on the measured displacement parameters, and the resulting Debye temperatures are also analyzed using pair distribution function of total neutron scattering, as refined over varying distance ranges of the pair distribution function. The interplay between optimal bonding in the structure, structural rigidity, and correlated motion in these structures is examined, and the different contributions are delineated.

Keywords

1 Introduction

Phosphor-converted white light emitting diodes (PCLEDs) offer tremendous energy savings over traditional light sources due to high efficiency, tunable color, and long lifetimes, with the additional benefit of using environmentally benign materials.[1,2] PCLEDs generally contain two components, a blue or near-UV LED chip and a rare-earth substituted phosphor or phosphors that convert the LED emission to longer wavelengths, producing broad spectrum white light emission. The phosphor is a crucial component, impacting the overall luminous efficacy, color temperature, color rendition, and thermal stability of the resulting white light.[3–5] The most appropriate phosphors for this application usually involve the broad and symmetry-allowed 4f to 5d transitions in Ce^{3+} or Eu^{2+} substituted in a host matrix such as an oxide, oxyfluoride, nitride, or oxynitride.[5] The energies associated with these transitions are strongly influenced by the crystal field splitting of the 5d levels due to the surrounding host structure. Therefore, the geometry and chemistry of the host material are critical in the selection of known phosphors and in the discovery of new phosphor materials for use in PCLED applications.

Until recently, a majority of new phosphors were identified through chemical substitution in known compounds,[5–8] with occasional high throughput searches of familiar parameter space.[9,10] An alternative, potentially more efficient method presented recently employs Density Functional Theory (DFT) to screen for new potential phosphor hosts with high photoluminescent quantum yield (PLQY).[11] It has been suggested by some of us that highly three-dimensionally connected structures, such as yttrium aluminum garnet (YAG), possesses high PLQY (>90%) — when substituted with appropriate amounts of Ce^{3+} — due to structural rigidity that limits, at measurement temperatures, accessible phonon modes that would lead to non-radiative quenching mechanisms.[11,12] Structural rigidity, however, is not easily quantified in a solid and can be difficult to capture as a single parameter. The Debye temperature (Θ_D) was identified previously,[11] as an useful proxy for structural rigidity. Θ_D is easily calculated within the quasi-harmonic Debye model using elastic

constants determined from *ab initio* calculations.[11] Within this framework, rare-earth substituted phosphor hosts are selected by searching through crystal structure databases (*e.g.*, Inorganic Crystal Structure Database (ICSD)) for compounds with a high Θ_D, in addition to certain other parameters associated with plausible chemistry. These parameters include elemental compositions that would withstand reaction conditions, dopant sites for the activator ion, and a sufficiently wide band gap.

Experimentally, Θ_D is obtained either from low temperature heat capacity measurements or from atomic displacement parameters determined from careful scattering (typically neutron) studies. The latter technique is usually associated with studies of monoatomic solids, and for more complex solids, a weighted average of the displacement parameters across all atoms in the unit cell has been found to yield agreement with other techniques.[12] Θ_D measured experimentally using these two methods for a number of phosphor hosts has been shown to agree well with values calculated from DFT-derived parameters.[12–15]

In this work, we explore the structural signatures of several known oxide phosphor hosts, through a careful examination of the average and local structure determined using time-of-flight neutron scattering (including total scattering) and synchrotron powder diffraction methods. The oxide hosts Ba_2SiO_4, $BaAl_2O_2$, $SrAl_2O_4$, and Y_2SiO_5 were studied using these scattering techniques and low-temperature heat capacity measurements. The Debye temperature has been obtained using parameters obtained from DFT calculations, and measured from isotropic atomic displacement parameters refined from 15 K neutron scattering data using both average and local structure techniques. Separately, Θ_D has been extracted from fitting the low temperature heat capacity measured between 1.8 K and 20 K. Pair distribution function analysis of neutron scattering data collected at 15 K has been performed to explore local *versus* long-range rigidity, as described by the impact of correlated motion on the extracted Debye temperature. Finally, structural rigidity has been correlated with the ability of the different structure types to best optimize bonding

4

around the countercations that provide the substitution sites for the phosphor activator ions.

2 Experimental

Samples of Ba_2SiO_4, $BaAl_2O_4$, $SrAl_2O_4$, and Y_2SiO_5 were prepared by conventional high temperature solid-state reaction using starting materials of $BaCO_3$ (Materion, 99.9%), $SrCO_3$ (Aldrich, 99.9%), Y_2O_3 (Materion, 99.9%), CeO_2 (99.99% purity, Alfa Aesar), SiO_2 (Johnson Matthey, 99.9%), and Al_2O_3 (Sigma-Aldrich, 99.99%). Powders were intimately mixed using an agate mortar and pestle for approximately 30 minutes, pressed into pellets, and placed in dense alumina crucibles on a bed of sacrificial powder to prevent contact with the crucible. Samples were heated in a reducing atmosphere of 5% H_2/95% N_2 with heating and cooling ramps of 3 °C/min. and 4 °C/min, respectively, at 1350 °C for 4 h for Ba_2SiO_4, 1600 °C for 12 h for $BaAl_2O_4$, 1400 °C for 12 h for $SrAl_2O_4$, and 1400 °C for 12 h for Y_2SiO_5.

High-resolution synchrotron X-ray powder diffraction data were collected on the 11-BM instrument at the Advanced Photon Source (APS) at Argonne National Laboratory, at a temperature of 300 K using an average wavelength of $\lambda = 0.413742$ Å. Neutron powder diffraction data were collected using the NPDF instrument at the Los Alamos Neutron Science Center at Los Alamos National Laboratory. Samples were placed in vanadium containers, and time-of-flight neutron data was collected at 300 K and 15 K from four detector banks located at $\pm46°$, $\pm90°$, $\pm119°$, and $\pm148°$. Rietveld analysis was carried out using the General Structure Analysis System (GSAS).[16,17] Simultaneous refinements of the X-ray and neutron scattering data collected at 300 K were completed by adjusting the profile shapes and backgrounds (shifted Chebyshev function for X-ray, power series for neutron), refining neutron absorption coefficients, and adjusting the instrument parameters. These parameters were then kept static, and the X-ray data only was used to refine the unit cell

parameters. Both X-ray and neutron data were then used to refine the atomic positions. Then only neutron data was used to refine the atomic displacement parameters. Refinements of low temperature data were completed using only neutron powder diffraction data collected at 15 K. Crystal structures were visualized using the software VESTA.[18]

Density Functional Theory (DFT) calculations were performed using the Vienna *ab initio* Simulation Package (VASP 5.3)[19–22] within the projector augmented wave method (PAW).[23,24] Initial relaxation of the atomic positions were performed until the residual forces were $<1 \times 10^{-2}$ eV/Å. Exchange and correlation were described by Perdew-Burke-Ernzerhof using the generalized gradient approximation (GGA-PBE).[25] The energy cut-off of the plane wave basis set and the number of **k**-points used for each calculation are detailed in the Supporting Information. The bulk modulus and Poisson ratio were calculated as described previously[11] using the Voigt-Reuss-Hill (VRH) approximation[26] from the stress-strain relationship driven by ± 0.015 Å displacements.[27] The elastic moduli were then used to estimate the Debye temperature (Θ_D) using the quasi-harmonic Debye model.[11,28–30]

Debye temperatures for crystallographically distinct atoms, $\Theta_{\mathrm{D},i}$ were calculated from isotropic atomic displacement parameters using the low-temperature approximation:[31]

$$\Theta_{\mathrm{D},i} = \frac{3\hbar^2 N_A}{4k_\mathrm{B} M U_{iso,i}} \tag{1}$$

where i represents the atomic species Ba, Sr, Y, Si, Al, or O, M is the atomic weight of the atom, and $U_{iso,i}$ the isotropic atomic displacement parameter of the individual atomic species in the unit cell. The overall Debye temperature, Θ_D, was found by taking the weighted average of $\Theta_{\mathrm{D},i}$ from each atomic species, according to their Wyckoff multiplicities in the unit cell:

$$\Theta_\mathrm{D} = \frac{\sum m_i \Theta_{\mathrm{D},i}}{\sum m_i} \tag{2}$$

6

where m_i is the Wyckoff multiplicity of the individual atomic species.

Low-temperature heat capacity was measured using a Quantum Design Physical Properties Measurement System. Heat capacity measurements from 1.8 K to 20 K were collected on pellets with a mass of approximately 15 mg and analyzed using thermal relaxation calorimetry. A thin layer of Apiezon-N grease was used to ensure thermal contact between the platform and the sample. The heat capacity of the Apiezon-N grease was collected separately and subtracted from the measured sample heat capacity. The Θ_D was then extracted by fitting the heat capacity to the Debye model in the low-temperature limit:

$$C_p \approx \frac{12 N k_\mathrm{B} \pi^4}{5} \left(\frac{T}{\Theta_\mathrm{D}} \right)^3 \tag{3}$$

where N is the number of atoms per formula unit multiplied by the Avogadro number, k_B is the Boltzmann constant, and T is the temperature.

Pair distribution function (PDF) analysis was performed on the neutron powder diffraction data collected at 15 K. The data were extracted using PDFgetN[32] with $Q_{max} = 25\,\text{Å}$, $Q_{max} = 40\,\text{Å}$, $Q_{max} = 25\,\text{Å}$, and $Q_{max} = 40\,\text{Å}$ for Ba_2SiO_4, $BaAl_2O_4$, $SrAl_2O_4$, and Y_2SiO_5, respectively, based on data quality and collection time. Least-squares refinements were performed on the PDF to obtain local structure information using PDFgui.[33] The real-space instrument parameters Q_{damp} and Q_{broad} were determined from a crystalline material calibration standard and fixed at $0.00623\,\text{Å}^{-1}$ and $0.0021\,\text{Å}^{-1}$, respectively. Refinement ranges of 1 Å to r_{max}, with $r_{max} = 5\,\text{Å}$, 10 Å, 15 Å, 20 Å, and 50 Å, were chosen to explore the effects of diffuse thermal scattering and correlated motion on the local structure and the average structure. Crystal structure depcitions and calculations of distance and distortion parameters were carried out using the VESTA suite of programs.[18]
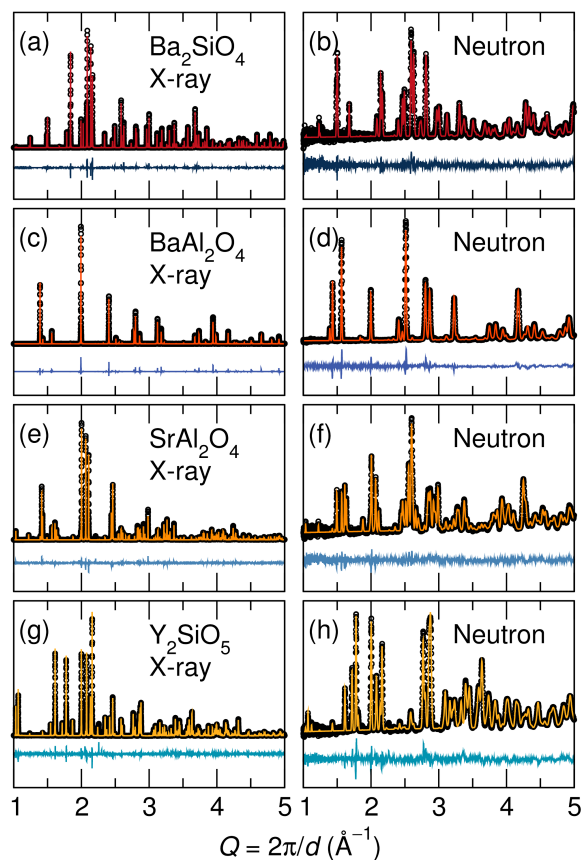
Figure 1: Rietveld co-refinements of combined high resolution synchrotron X-ray diffraction from beam line 11-BM (left) and neutron powder diffraction from the NPDF instrument (right) collected at 300 K for (a,b) Ba_2SiO_4, (c,d) $BaAl_2O_4$, (e,f) $SrAl_2O_4$, and (g,h) Y_2SiO_5. The small circles are measured data and solid lines the fit, with the differences displayed beneath. Neutron data presented here is from from bank 1.
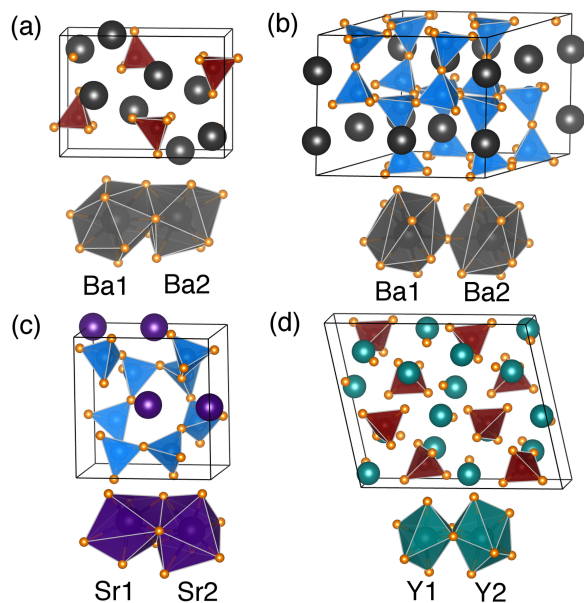
Figure 2: Crystal structure and polyhedral coordination environment for (a) Ba_2SiO_4, (b) $BaAl_2O_4$, (c) $SrAl_2O_4$, and (d) Y_2SiO_5 refined from combined high resolution synchrotron X-ray and neutron powder diffraction data collected at 300 K. The alkaline-earth and rare-earth cations are depicted as large spheres, while Si and Al are situated in the centers of the rendered SiO_4 and AlO_4 polyhedra (tetrahedra).

3 Results and Discussion

The host structures Ba_2SiO_4, $BaAl_2O_4$, $SrAl_2O_4$, and Y_2SiO_5 were chosen for this study to explore the effects of various connectivity, coordination, and composition on structural rigidity. Upon Ce^{3+} substitution, these structures all exhibit photoluminescence from two crystallographically distinct sites in the host structure, occurring in the near-UV to visible spectrum, although their luminescent properties are not the focus of this study. Simultaneous co-refinements of high resolution synchrotron X-ray and neutron power diffraction data collected at 300 K were conducted using the undoped host materials in order to describe the average structure of these compounds at room temperature. Figure 1 shows the fits against both the X-ray data and the neutron data with good agreement between the data and the structural model. The crystallographic refinement data for all compounds are listed in the Supporting Information. The crystal structures are illustrated in Figure 2.

Ba_2SiO_4 crystallizes in the orthorhombic space group $Pmcn$ (No. 62) with the β-K_2SO_4

9

structure type, containing isolated SiO_4 tetrahedra.[34] $BaAl_2O_4$ and $SrAl_2O_4$ are derivatives of the tridymite structure in space group $P6_3/mmc$ (No. 194), where the Ba^{2+} and Sr^{2+} ions are situated in the channels created by the tridymite-related AlO_4 tetrahedral corner connected network. $BaAl_2O_4$ was first reported in 1937 in the hexagonal space group $P6_322$ (No. 182), but since that time the observation of satellite reflections in X-ray diffraction data have suggested a superstructure doubling of the a and b lattice parameters, resulting in space group $P6_3$ (No. 173).[35] There has been some discussion around whether this description is only an average structure description, and the local structure may instead more closely resemble the monoclinic $P2_12_12_1$ (No. 19) or the monoclinic $P2_1$ (No. 4) structure in which $SrAl_2O_4$ crystallizes.[36,37] In this study, we have found the hexagonal space group $P6_3$ (No. 173) structural model, with the $KNa_3Al_4Si_4O_{16}$ structure type, to fit both the high and low temperature average and local structure. This model has been used for all subsequent refinements of $BaAl_2O_4$. $BaAl_2O_4$ contains AlO_4 dimers while the AlO_4 units in $SrAl_2O_4$ are fully connected in three dimensions.

Y_2SiO_5 crystallizes in the low temperature X_1 structure in the monoclinic space group $P2_1/c$ (No.14) and the high temperature X_2 structure in the monoclinic space group $I2/a$ (No. 15). The high temperature X_2 structure has been reported to have stronger luminescence compared to the X_1 structure type.[38] In this study, we have refined the X_2 structural model with the $(Mn,Fe)_2PO_4F$ structure type, containing isolated SiO_4 tetrahedra, and thus have used this model for all subsequent refinements of Y_2SiO_5.

Table 1: Comparison of effective ionic radii indicates potential substitution sites for Ce^{3+} in different coordination geometries.

CN	atom	effective ionic radii (Å)	Ce^{3+} effective ionic radii (Å)
9	Ba^{2+}	1.47	1.196
10	Ba^{2+}	1.52	1.25
7	Sr^{2+}	1.21	1.07
8	Sr^{2+}	1.26	1.143
6	Y^{3+}	0.90	1.01
7	Y^{3+}	0.96	1.07

Table 2: Structural information of the potential sites for Ce^{3+} substitution from Rietveld co-refinements of combined high resolution synchrotron X-ray and neutron powder diffraction data collected at 300 K including site, coordination number (CN), average bond length, polyhedral volume, polyhedral distortion index D, and bond valence sum (BVS).

sample	site	CN	ave. bond length (Å)	poly. vol. (Å^3)	D	BVS
Ba_2SiO_4	Ba1 $4c$	10	2.984	53.214	0.0445	1.675
	Ba2 $4c$	9	2.828	43.210	0.0466	2.254
$BaAl_2O_4$	Ba1 $2a$	9	2.921	43.000	0.0388	1.706
	Ba2 $6c$	9	2.955	44.783	0.0575	1.682
$SrAl_2O_4$	Sr1 $2a$	7	2.680	26.240	0.0465	1.684
	Sr2 $2a$	8	2.749	33.296	0.0734	1.743
Y_2SiO_5	Y1 $8f$	6	2.272	14.536	0.0078	3.039
	Y2 $8f$	7	2.361	18.782	0.0330	2.902

Table 1 compares the effective ionic radii of the potential activator ion Ce^{3+} in different coordination environments with the effective ionic radii of cations in the host structure that represent possible substitution sites.[39] Comparison of effective ionic radii indicates that all of the structures contain two potential substitution sites for Ce^{3+}, Table 2 lists the characteristics of the coordination environments. Since the bonding environment of these cation sites will influence the activator ion energy levels and in turn the optical properties, we have focused on an analysis of these coordination environments. The polyhedral volume of the sites were calculated using the method outlined by Swanson and Peterson.[40] A polyhedral distortion index, D, can also be calculated following[41]

$$D = \frac{1}{n} \sum_{i=1}^{n} \frac{\mid l_i - l_{av} \mid}{l_{av}} \qquad (4)$$

where l_i is the distance from the central atom to the ith coordinating atom and l_{av} is the average bond length. The polyhedra of each of the two cation sites in each structure is illustrated in Figure 2 with the refined crystal structures.

The two Ba–O polyhedra in Ba_2SiO_4 have strikingly different coordination environments. There exists a larger, under-bonded 10-coordinated Ba1 site and a smaller, over-bonded and structurally distorted 9-coordinated Ba2 site. In the $BaAl_2O_4$ structure, both

11

Ba^{2+} sites are 9-coordinated and under-bonded, with the volume of the Ba2 site slightly larger but more distorted compared to Ba1. SrAl$_2$O$_4$ exhibits two Sr sites that are both under-bonded, with the Sr2 site having a slightly larger volume, but also more distorted coordination than the Sr1 site. In Y$_2$SiO$_5$, there exists a smaller, over-bonded, but less distorted 6-coordinated Y1 site and a larger, under-bonded 7-coordinated Y2 site.

Table 3: Debye temperature calculated using density functional theory, measured using atomic displacement parameters from Rietveld refinement of neutron scattering data collected at 15 K, low temperature heat capacity collected at 1.8 K, and atomic displacement parameters from PDF analysis of neutron scattering data collected at 15 K refined from 1 Å to 50 Å.

sample	Θ_D (K)			
technique	DFT	Rietveld U_{iso}	C_p	PDF U_{iso}
Ba$_2$SiO$_4$	305	311	305	294
BaAl$_2$O$_4$	354	377	316	387
SrAl$_2$O$_4$	475	352	455	430
Y$_2$SiO$_5$	513	500	419	350

Density functional theory (DFT) provides a method for predicting Θ_D, which is indicative of structural rigidity in phosphor hosts.[11] This method was used to calculate Θ_D for each compound using the structure determined from room temperature co-refinements. Θ_D results are listed in Table 3. Based on Pauling's rules for ionic crystal structures,[42] we would expect that structures containing polyhedra of lower charge cations (Al^{3+} instead of Si^{4+}) and oxygen would be better connected and therefore more rigid, and this is indeed borne out by the DFT calculations.

Ba$_2$SiO$_4$ contains isolated SiO$_4$ tetrahedra and a divalent cation with the largest co-ordination numbers for this series of compounds explored, producing the lowest Θ_D. BaAl$_2$O$_4$ and SrAl$_2$O$_4$ contain similar elements but different AlO$_4$ connectivity. BaAl$_2$O$_4$ contains corner-connected AlO$_4$ dimers, while in SrAl$_2$O$_4$ AlO$_4$ tetrahedra are fully three-dimensionally connected. The higher degree of connectivity in SrAl$_2$O$_4$ leads to the higher Θ_D, as observed. Finally, Y$_2$SiO$_5$ contains isolated SiO$_4$ tetrahedra; however the higher cation charge of yttrium compared to barium or strontium leads to stronger bonding and
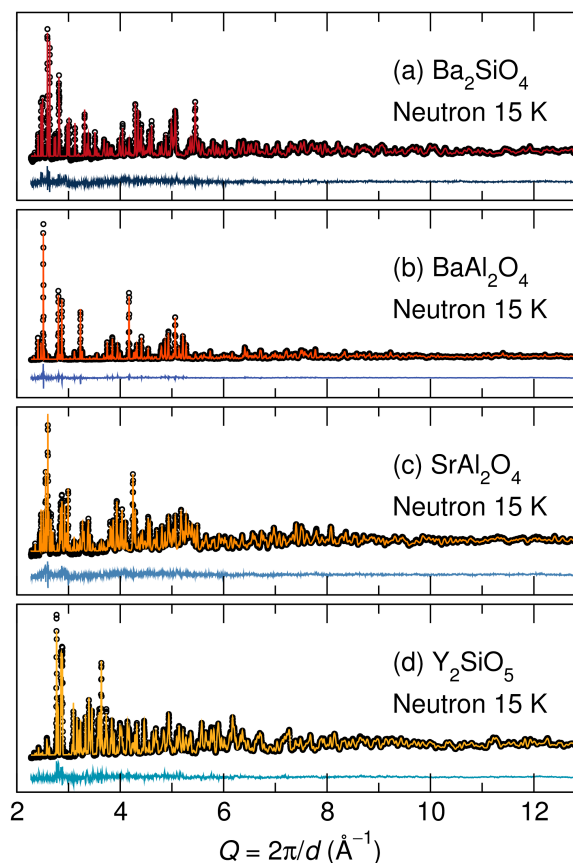
a higher Θ_D.

Figure 3: Rietveld refinements of low temperature neutron powder diffraction data collected at 15 K and normalized, for (a) Ba_2SiO_4, (b) $BaAl_2O_4$, (c) $SrAl_2O_4$, and (d) Y_2SiO_5. Circles represent the data and solid lines the fit, with the difference beneath.

Refinements of low temperature neutron power diffraction data collected at 15 K were conducted to extract atomic displacement parameters (U_{iso}) to experimentally determine Θ_D. Figure 3 shows excellent agreement between the structural models and the data. The crystal data and refinement information are listed in the Supporting Information.

The coordination environment of each potential site for Ce^{3+} substitution are listed in Table 4 for the low temperature structural refinements. The crystal structures, illustrated in Figure 4, show 99% probability U_{iso} ellipsoids.

The Θ_D is then determined from U_{iso} for each structure using the equations described previously, with results listed in Table 3. The experimentally determined Θ_D agrees well (±25 K) for all compounds except $SrAl_2O_4$. For $SrAl_2O_4$, the experimentally determined

13

Table 4: Polyhedral information of the potential sites for Ce^{3+} substitution from Rietveld refinements of neutron powder diffraction data collected at 15 K including site, coordination number (CN), average bond length, polyhedral volume, polyhedral distortion index D, and bond valence sum (BVS).

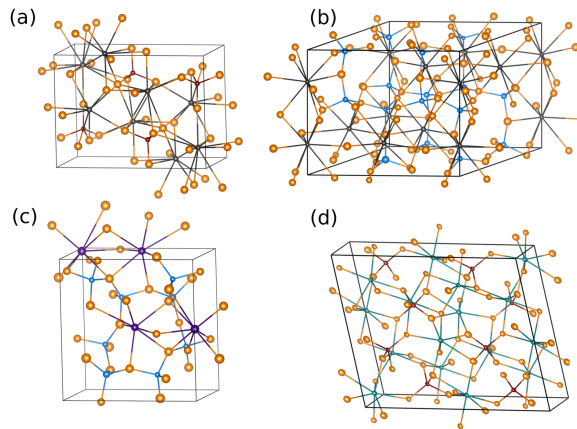| sample	site	CN	bond length (Å)	poly. vol. (Å^3)	D	BVS
Ba_2SiO_4	Ba1 $4c$	10	2.973	52.585	0.0462	1.735
	Ba2 $4c$	9	2.816	42.753	0.0456	2.313
$BaAl_2O_4$	Ba1 $2a$	9	2.897	41.837	0.0289	1.773
	Ba2 $6c$	9	2.954	44.569	0.0660	1.788
$SrAl_2O_4$	Sr1 $2a$	7	2.670	26.005	0.0472	1.728
	Sr2 $2a$	8	2.732	32.994	0.0707	1.800
Y_2SiO_5	Y1 $8f$	6	2.268	14.458	0.0080	3.072
	Y2 $8f$	7	2.355	18.645	0.0316	2.944

Figure 4: Crystal structures showing 99% probability atomic displacement parameters for (a) Ba_2SiO_4, (b) $BaAl_2O_4$, (c) $SrAl_2O_4$, and (d) Y_2SiO_5 refined using low temperature neutron powder diffraction data collected at 15 K.

Θ_D from U_{iso} is lower than predicted by the DFT calculations. This disagreement could result from static disorder in the average $SrAl_2O_4$ crystal structure, contributing to larger than expected atomic displacements and a low Θ_D. Based on the pair distribution (PDF) analysis presented in what follows, Θ_D from PDF U_{iso} fit over the range of 1 Å to 50 Å, also representing the average structure, is determined to be 430 K. This result is higher than estimated from the average structure Rietveld analysis and supports static disorder as a cause for the lower than expected Θ_D.
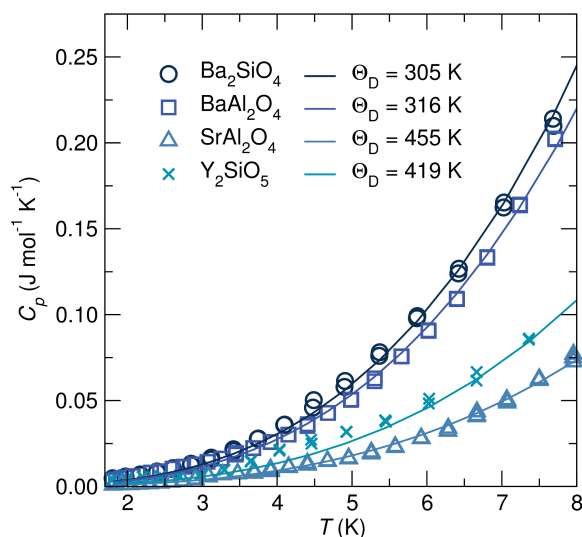

Figure 5: Low temperature heat capacity with extracted Debye temperatures for Ba_2SiO_4, $BaAl_2O_4$, $SrAl_2O_4$, and Y_2SiO_5.

Low-temperature heat capacity measurements were also performed to experimentally determine Θ_D. The heat capacities (C_p) of Ba_2SiO_4, $BaAl_2O_4$, $SrAl_2O_4$, and Y_2SiO_5 were collected at temperatures as low as 1.8 K and are shown in Figure 5. The data were fit to the Debye model, in the linear region of the log-log plot, and the extracted Θ_D are listed in Table 3. While the Debye model was fit very well to the heat capacity of other compounds from 3 K to 8 K, an anomaly in the heat capacity of Y_2SiO_5 prevents appropriate use of the simple Debye model below 5 K, and makes the measured value for this compound somewhat less than reliable. A plot of C_p/T^3 *vs.* T for Y_2SiO_5 reveals a peak ranging from 3 K to 6 K, well within the low temperature fitting range, pointing towards the presence of

15

localized, optic-like modes. One possibility for the anomaly at low temperatures in Y_2SiO_5 are Van Hove singularities arising from the vibrational density of states (VDOS) crossing the Debye density of states, leading to a flat phonon dispersion curve.[43,44] Since the T^3 Debye model only accounts for low-frequency phonon contributions to the specific heat, and breaks down when temperatures exceed between *e.g.*, $T > \Theta_D/50$ to $\Theta_D/100$,[45,46] the use of the higher-temperature data leads to a lower-than-expected Θ_D determined for Y_2SiO_5.
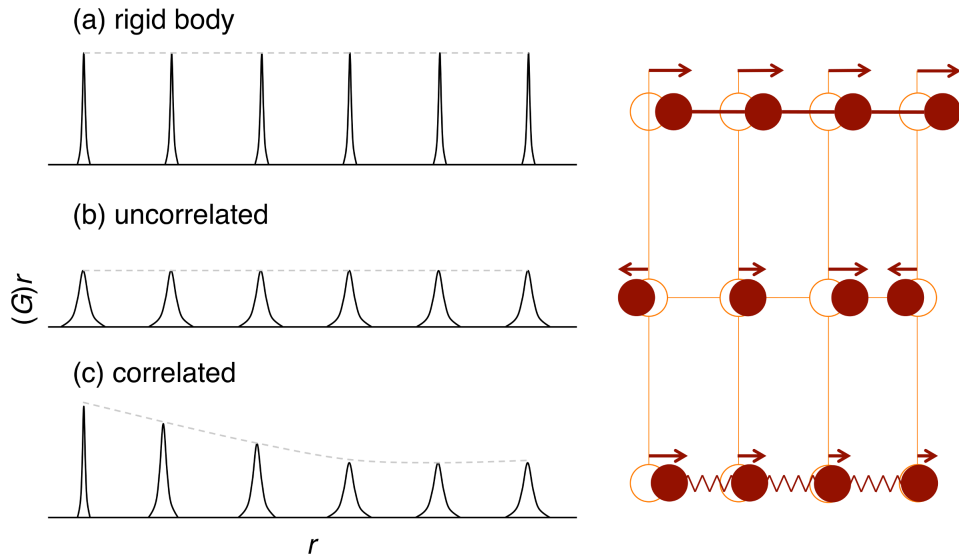

Figure 6: A visualization of the impact of correlated atomic motion on the pair distribution function. (a) Rigid body motion as depicted using a chain of atoms can be expected to give δ-function peaks in the PDF of the infinite crystal. (b) Completely uncorrelated motion as associated with Einstein modes should yield PDF peaks whose widths do not vary with increasing distance. (c) Correlated motion combines the features of (a) and (b). Adapted with permission from Jeong *et al.*[47] Copyright (2003) American Physical Society.

Understanding the local structure of phosphor hosts is crucially important to understanding their resultant optical properties. In addition, understanding long-range and short-range structural rigidity may provide further insights into the role of structural rigidity in phosphors. Pair distribution function (PDF) analysis is one method that can be used to study the local structure of phosphor hosts. In this study, we have analyzed the PDF of the low temperature neutron powder diffraction data collected at 15 K, and determined Θ_D from refined U_{iso}. The PDFs were fit over different real-space r_{max}-ranges to evaluate

the effects of thermal diffuse scattering and static disorder on the measured Θ_D and to evaluate the role of correlated motion.

The correlated motion of atoms and its impact on the PDF is depicted in Figure 6. Rigid-body thermal motion contains atoms moving the same distance and in the same direction as the atom being observed, which is represented in a PDF as a series of sharp peaks for all distances from the atom or ranges of r. In uncorrelated atomic motion, all atoms move independently of the atom being observed, which is represented as a series of broad peaks for all ranges of r. Correlated atomic motion in the PDF is a combination of the observations where the local structure may not translate into the average, long-range structure. This is represented in a PDF as sharp peaks at low-r, similar to rigid-body thermal motion, and broad peaks at high-r, similar to uncorrelated atomic motion. This correlated motion is captured in the PDF by the empirical parameters δ_1 and δ_2, often used for high temperature and low temperature behavior, respectively. The final PDF peak width is given by:[47,48]

$$\sigma_{ij} = \sigma'_{ij}\sqrt{1 - \frac{\delta_1}{r_{ij}} - \frac{\delta_2}{r_{ij}^2} + Q_{broad}^2 r_{ij}^2} \tag{5}$$

where σ'_{ij} is the peak width without correlation, computed from U_{iso}. The degree of correlated motion within a material is dictated by both interatomic interactions and atomic geometry based on crystal structure.

The PDFs were first fit over the range of $1\,\text{Å}$ to $50\,\text{Å}$ to refine the low temperature δ_2 correlated motion parameter. This fit range represents the long-range, average structure. Then, δ_2 was fixed and the data were fit over subsequently lower ranges of r_{max}, including $1\,\text{Å}$ to $20\,\text{Å}$, $1\,\text{Å}$ to $15\,\text{Å}$, $1\,\text{Å}$ to $10\,\text{Å}$, and $1\,\text{Å}$ to $5\,\text{Å}$. Refinements of the PDFs fit over the range of $1\,\text{Å}$ to $20\,\text{Å}$ are illustrated in Figure 7 for all host structures with good agreement between the structural model and the data. Fits to the PDF for all r_{max}-ranges are shown in the Supporting Information.

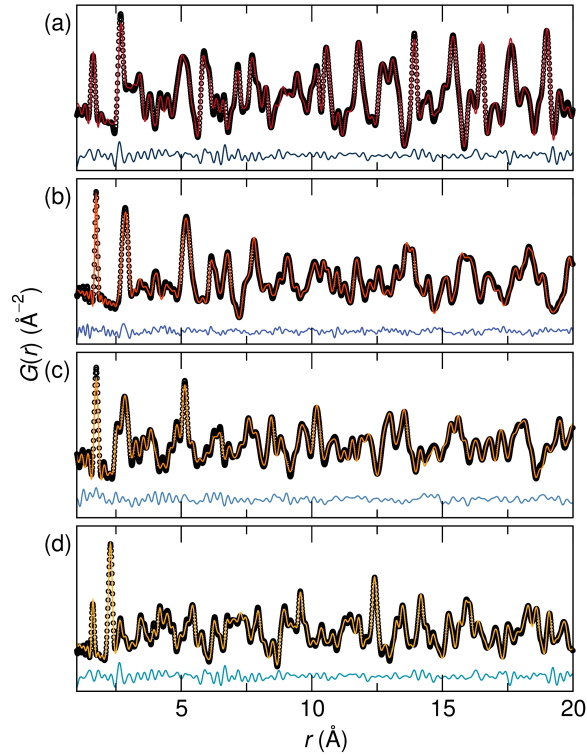The correlated motion parameter, δ_2, is refined to be $2.35\,\text{Å}^2$, $2.78\,\text{Å}^2$, $2.79\,\text{Å}^2$, and

Figure 7: Least squares refinements of the pair distribution function of (a) Ba_2SiO_4, (b) $BaAl_2O_4$, (c) $SrAl_2O_4$, and (d) Y_2SiO_5 from low temperature neutron powder diffraction data collected at 15 K and fit from 1 Å to 20 Å. Circles represent the data and solid lines the fit, with the differences beneath.
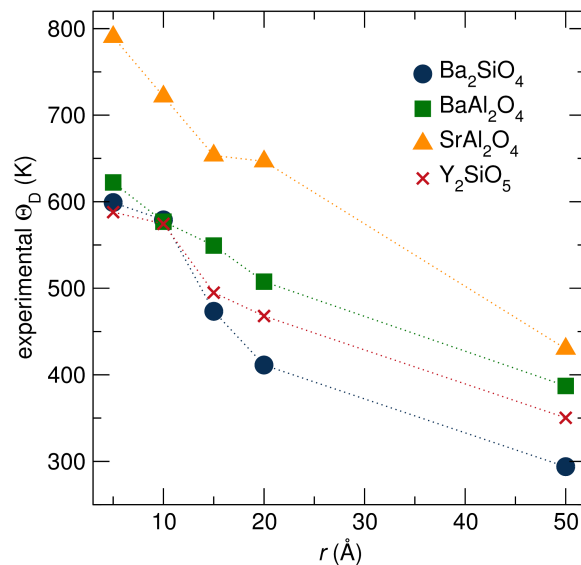

Figure 8: Θ_D as a function of fitting range r_{max} determined from atomic displacement parameters refined using the pair distribution function of the neutron diffraction data collected at 15 K.

2.52 Å^2 for Ba$_2$SiO$_4$, BaAl$_2$O$_4$, and SrAl$_2$O$_4$, and Y$_2$SiO$_5$, respectively. The correlated motion parameter should be representative of the degree of structural rigidity in a material and thus associated with the Θ_D. We find that the degree of correlated motion follows closely the degree of structural connectivity, as discussed earlier. Ba$_2$SiO$_4$ and Y$_2$SiO$_5$ contain isolated SiO$_4$ tetrahedra and a lower correlated motion parameter compared to the AlO$_4$ dimers and three-dimensionally connected AlO$_4$ tetrahedra in BaAl$_2$O$_4$ and SrAl$_2$O$_4$, respectively.

The PDF peak width modeled using U_{iso} contains information on both the thermal diffuse scattering and static disorder. Fitting the PDF over varying r_{max}-ranges can be used to evaluate the effects of thermal diffuse scattering. It will be manifested as significantly smaller U_{iso} for short-range modeling (lower r) where the effects of the averaged thermal diffuse scattering are minimized.[49] Θ_D for each r_{max}-range determined using U_{iso} from PDF refinements are shown in Figure 8. The Θ_D determined from refined U_{iso} from the PDF is higher in the low-r region, corresponding to the local structure, decreasing with increasing r_{max}-range, as r approaches the average structure description.

In the low-r region for $r_{max} = 5$ Å, it is the local structure of the first coordination shell of the polyhedra being observed. This is a useful range for observing the local rigidity that may influence optical properties pertaining to specific crystallographic sites and activator ion substitution. For example, we would expect this local rigidity to affect expansion or contraction, and distortion, of the lattice that may or may not occur with activator ion substitution. This could have implications as to why specific activator ions have optimal performance in certain structures and how this affects optical properties like quantum yield and Stokes shift.

As r_{max} increases, Θ_D decreases, gaining contributions from the long-range thermal diffuse scattering and interactions from the lattice as a whole. In the high-r region of r_{max} = 50 Å, corresponding to the long-range average structure, Θ_D agrees well (± 45 K) with values determined using other average structure techniques, and are listed in Table 3. The

Θ_D for Y_2SiO_5 is somewhat lower than expected, which may be influenced by the lower than expected correlated motion parameter included in the refinement.
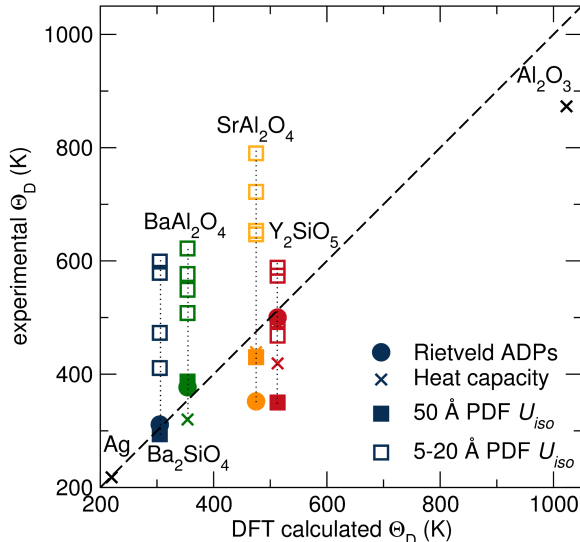

Figure 9: Calculated Θ_D from DFT and experimental Θ_D determined using atomic displacement parameters from Rietveld and PDF refinements of low temperature neutron powder diffraction data collected at 15 K, and extracted from low temperature heat capacity collected at 1.8 K for all compositions. The different datapoints for the PDF refinements indicate increasing values of r_{max}, with the trend that the PDF-calculated Debye temperature for sample decreases with increasing r_{max}. Also included as a reference are the Θ_D for silver and alumina measured using the low temperature heat capacity method.

Figure 9 shows the Θ_D determined from the four methods used: DFT calculated, experimentally measured from Rietveld refined U_{iso} from 15 K neutron powder diffraction data, from low temperature heat capacity measurements, and from PDF U_{iso} refined from 15 K neutron powder diffraction data fit over varying ranges of r_{max}. Also included as a reference are the Θ_D for silver and alumina measured using the low temperature heat capacity method discussed here.

For those materials where the local structure Θ_D decreases drastically to the average structure Θ_D, there is a large amount of thermal diffuse scattering present. Figure 10a shows the difference in measured Θ_D from the local structure 1 Å to 5 Å PDF fit range to the DFT calculated Θ_D as a percentage of the expected DFT calculated Θ_D. We find that, for the compounds studied here, this large change from local to average Θ_D corresponds
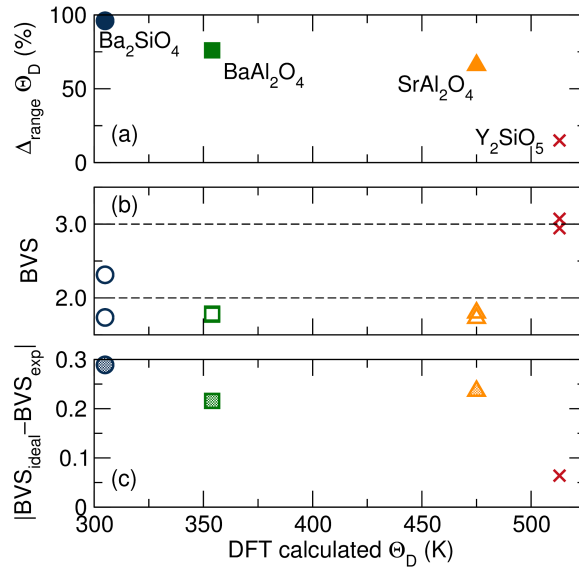
20

Figure 10: (a) The difference in measured Θ_D from the local structure 1 Å to 5 Å PDF fitting range and the average structure DFT calculated Θ_D as a percentage of the expected DFT calculated Θ_D, (b) the bond valence sums (BVS) for each cation site in each composition determined from Rietveld refinement of neutron diffraction data collected at 15 K showing the deviation from ideal $2+$ for Ba^{2+} and Sr^{2+} and ideal $3+$ for Y^{3+}, and (c) the average deviation from ideal bond valence sums weighted by site multiplicity shows that for more optimized structures the changes in measured Θ_D as a function of PDF fitting range and the difference in bond valence sum from ideal is smaller, coinciding with higher Θ_D materials.

with a low Θ_D.

We also find that the thermal diffuse scattering measured through PDF analysis and resulting Θ_D can be related to the structural parameters refined using average structure techniques as an indication of average structural rigidity. Figure 10b shows the bond valence sum (BVS) determined for each of the two cation sites in each structure compared to the predicted BVS of 2+ for Ba^{2+} and Sr^{2+} and 3+ for Y^{3+}. Figure 10c shows the average difference between the ideal BVS and experimental BVS for each site, based on multiplicity. We find that for materials that are optimally bonded, the distance from the ideal BVS is small and the difference in measured Θ_D as a function of pdf fit range is also small, representing a material with high structural rigidity and a high Θ_D. The Θ_D can therefore be considered a measure of rigidity for the average structural description, whereas local structures techniques like PDF can be used to determine the rigidity of the local structure using a description of correlated motion or a local structure Θ_D, which may provide future insights as to the role of local structural rigidity in phosphor compounds.

4 Conclusions

The results presented here explore the role of structural rigidity in several oxide structures as host materials for phosphors used in solid-state lighting. The average structures of Ba_2SiO_4, $BaAl_2O_4$, $SrAl_2O_4$, and Y_2SiO_5 are determined through simultaneous refinements of synchrotron X-ray diffraction and neutron scattering. The Debye temperature (Θ_D) is used as a proxy to quantify structural rigidity and is predicted using Density Functional Theory (DFT) calculations in agreement with qualitative analysis of the structures based Pauling's rules for ionic crystals. The Θ_D is then measured experimentally using refined atomic displacement parameters (U_{iso}) from neutron scattering data collected at $15\,\mathrm{K}$ and extracted from low temperature heat capacity measurements. The rigidity of the local structure *versus* the average structure is then explored by analyzing the effects of

correlated motion and diffuse thermal scattering on the pair distribution function (PDF) obtained from 15 K neutron scattering. Correlated motion in the PDF appears stronger for structures with a higher degree of connectivity and the difference in Θ_D corresponding to the local structure compared to the average structure varies based on the degree of diffuse thermal motion present. For highly rigid structures, the difference in Θ_D from the local to the average structure is small, indicating little thermal motion, and coinciding with high calculated Θ_D and ideal bond valence sums determined from analysis of the average structure. Additionally, rigidity of the local structure may present an avenue for understanding the effects of activator ion substitution on the host structure and its impacts on the optical properties.

Acknowledgement

Supporting Information Available

Crystal data, fitting statistics, and refined atomic parameters from Rietveld refinements for all compounds and least squares refinements of the pair distribution function for all compounds. This material is available free of charge via the Internet at `http://pubs.acs.org/`.

References

(1) Hashimoto, T.; Wu, F.; Speck, J. S.; Nakamura, S. A GaN Bulk Crystal with Improved Structural Quality Grown by the Ammonothermal Method. *Nature Mater.* **2007**, *6*, 568–571.

(2) Pimputkar, S.; Speck, J. S.; DenBaars, S. P.; Nakamura, S. Prospects for LED Lighting. *Nature Photonics* **2009**, *3*, 180–182.

(3) Jüstel, T.; Nikol, H.; Ronda, C. New Developments in the Field of Luminescent Materials for Lighting and Displays. *Angew. Chem. Int. Ed.* **1998**, *37*, 3084–3103.

(4) Schubert, E. F.; Kim, J. K. Solid-State Light Sources Getting Smart. *Science* **2005**, *308*, 1274–1278.

(5) George, N. C.; Denault, K. A.; Seshadri, R. Phosphors for Solid-State White Lighting. *Annu. Rev. Mater. Res.* **2013**, *43*, 481–501.

(6) Im, W. B.; Brinkley, S.; Hu, J.; Mikhailovsky, A.; DenBaars, S. P.; Seshadri, R. $Sr_{2.975-x}Ba_xCe_{0.025}AlO_4F$: A Highly Efficient Green-Emitting Oxyfluoride Phosphor for Solid State White Lighting. *Chem. Mater.* **2010**, *22*, 2842–2849.

(7) Im, W. B.; George, N.; Kurzman, J.; Brinkley, S.; Mikhailovsky, A.; Hu, J.; Chmelka, B. F.; DenBaars, S. P.; Seshadri, R. Efficient and Color-Tunable Oxyfluoride Solid Solution Phosphors for Solid-State White Lighting. *Adv. Mater.* **2011**, *23*, 2300–2305.

(8) Denault, K. A.; George, N. C.; Paden, S. R.; Brinkley, S.; Mikhailovsky, A. A.; Neuefeind, J.; DenBaars, S. P.; Seshadri, R. A Green-Yellow Emitting Oxyfluoride Solid Solution Phosphor $Sr_2Ba(AlO_4F)_{1-x}(SiO_5)_x$:$Ce^{3+}$ for Thermally Stable, High Color Rendition Solid State White Lighting. *J. Mater. Chem.* **2012**, *22*, 18204–18213.

(9) Danielson, E.; Golden, J. H.; McFarland, E. W.; Reaves, C. M.; Weinberg, W. H.; Wu, X. D. A Combinatorial Approach to the Discovery and Optimization of Luminescent Materials. *Nature* **1997**, *389*, 944–948.

(10) Sohn, K.-S.; Park, D. H.; Cho, S. H.; Kim, B. I.; Woo, S. I. Genetic Algorithm Assisted Combinatorial Search for a New Green Phosphor for Use in Tricolor White LEDs. *J. Combi. Chem.* **2006**, *8*, 44–49.

(11) Brgoch, J.; DenBaars, S. P.; Seshadri, R. Proxies From Ab Initio Calculations for Screening Efficient Ce^{3+} Phosphor Hosts. *J. Phys. Chem. C* **2013**, *117*, 17955–17959.

(12) George, N. C.; Pell, A. J.; Dantelle, G.; Page, K.; Llobet, A.; Balasubramanian, M.; Pintacuda, G.; Chmelka, B. F.; Seshadri, R. Local Environments of Dilute Activator Ions in the Solid-State Lighting Phosphor $Y_{3-x}Ce_xAl_5O_{12}$. *Chem. Mater.* **2013**, *25*, 3979–3995.

(13) Denault, K. A.; Brgoch, J.; Gaultois, M. W.; Mikhailovsky, A.; Petry, R.; Winkler, H.; DenBaars, S. P.; Seshadri, R. Consequences of Optimal Bond Valence on Structural Rigidity and Improved Luminescence Properties in $Sr_xBa_{2-x}SiO_4$:Eu^{2+} Orthosilicate Phosphors. *Chem. Mater.* **2014**, *26*, 2275–2282.

(14) George, N. C.; Birkel, A.; Brgoch, J.; Hong, B.-C.; Mikhailovsky, A. A.; Page, K.; Llobet, A.; Seshadri, R. Average and Local Structural Origins of the Optical Properties of the Nitride Phosphor $La_{3-x}Ce_xSi_6N_{11}$ $(0 < x \leq 3)$. *Inorg. Chem.* **2013**, *52*, 13730–13741.

(15) Brgoch, J.; Gaultois, M. W.; Balasubramanian, M.; Page, K.; Hong, B.-C.; Seshadri, R. Local Structure and Structural Rigidity of the Green Phosphor β-SiAlON:Eu^{2+}. *Appl. Phys. Lett.* **2014**, *105*, 181904 .

(16) Larson, A. C.; Von Dreele, R. B. General Structure Analysis System (GSAS). *Los Alamos National Laboratory Report LAUR* **2000**, 86–748.

(17) Toby, B. H. EXPGUI, A Graphical User Interface for GSAS. *J. Appl. Crystallogr.* **2001**, *34*, 210–213.

(18) Momma, K.; Izumi, F. VESTA3 for Three-Dimensional Visualization of Crystal, Volumetric and Morphology Data. *J. Appl. Crystallogr.* **2011**, *44*, 1272–1276.

(19) Kresse, G.; Hafner, J. Ab Initio Molecular Dynamics For Liquid Metals. *Phys. Rev. B* **1993**, *47*, 558.

(20) Kresse, G.; Hafner, J. Ab Initio Molecular-Dynamics Simulation of the Liquid-Metal-Amorphous-Semiconductor Transition in Germanium. *Phys. Rev. B* **1994**, *49*, 14251.

(21) Kresse, G.; Furthmüller, J. Efficiency of Ab-Initio Total Energy Calculations for Metals and Semiconductors Using a Plane-Wave Basis Set. *Comput. Mat. Sci.* **1996**, *6*, 15.

(22) Kresse, G.; Furthmüller, J. Efficient Iterative Schemes for Ab Initio Total-Energy Calculations Using a Plane-Wave Basis Set. *Phys. Rev. B* **1996**, *54*, 11169.

(23) Blöchl, P. E. Projector Augmented-Wave Method. *Phys. Rev. B* **1994**, *50*, 17953.

(24) Kresse, G.; Joubert, D. From Ultrasoft Pseudopotentials to the Projector Augmented-Wave Method. *Phys. Rev. B* **1999**, *59*, 1758.

(25) Perdew, J. P.; Burke, K.; Ernzerhof, M. Generalized Gradient Approximation Made Simple. *Phys. Rev. Lett.* **1996**, *77*, 3865.

(26) Hill, R. The Elastic Behaviour of a Crystalline Aggregate. *Phys. Soc. London* **1952**, *65*, 350.

(27) Le Page, Y.; Saxe, P. Elastic Constants in VASP. *Phys. Rev. B* **2002**, *65*, 104104.

(28) Francisco, E. and Recio, J. M. and Blanco, M. A. and Pendás, A. Martín and Costales, A., Quantum-Mechanical Study of Thermodynamic and Bonding Properties of MgF_2. *J. Phys. Chem. A* **1998**, *102*, 1595–1601.

(29) Francisco, E.; Blanco, M. A.; Sanjurjo, G. Atomistic Simulation of $\mathrm{SrF_2}$ Polymorphs. *Phys. Rev. B* **2001**, *63*, 094107.

(30) Poirier, J. *Introduction to the Physics of the Earth's Interior*; Cambridge University Press, 2000.

(31) Willis, B. T. M.; Pryor, A. W. *Thermal Vibrations in Crystallography*; Cambridge University Press, 1975.

(32) Peterson, P. F.; Gutmann, M.; Proffen, T.; Billinge, S. J. L. PDFgetN: A User-Friendly Program to Extract the Total Scattering Structure Factor and the Pair Distribution Function from Neutron Powder Diffraction Data. *J. Appl. Crystallogr.* **2000**, *33*, 1192–1192.

(33) Farrow, C. L. and Juhás, P. and Liu, J. W. and Bryndin, D. and Božin, E. S. and Bloch, J. and Proffen, Th. and Billinge, S. J. L., PDFfit2 And PDFgui: Computer Programs for Studying Nanostructure in Crystals. *J. Phys.-Condens. Mat.* **2007**, *19*, 335219.

(34) Grosse, H.; Tillmanns, E. Bariumorthosilicate, $\mathrm{Ba_2SiO_4}$. *Cryst. Struct. Commun.* **1974**, *3*.

(35) Larsson, A.-K.; Withers, R.; Perez-Mato, J.; Gerald, J. F.; Saines, P.; Kennedy, B.; Liu, Y. On the Microstructure and Symmetry of Apparently Hexagonal $\mathrm{BaAl_2O_4}$. *J. Solid State Chem.* **2008**, *181*, 1816 – 1823.

(36) Schulze, A.-R.; Buschbaum, H. M. Zur Verbindungsbildung von $\mathrm{MeO{:}M_2O_3}$. IV. Zur Struktur von Monoklinem $\mathrm{SrAl_2O_4}$. *Z. Anorg. Allg. Chem.* **1981**, *475*, 205–210.

(37) Avdeev, M.; Yakovlev, S.; Yaremchenko, A. A.; Kharton, V. V. Transitions Between $P2_1$, $P6_3(\sqrt{3a})$, and $P6_322$ Modifications of $\mathrm{SrAl_2O_4}$ by in situ High-Temperature X-Ray and Neutron Diffraction. *J. Solid State Chem.* **2007**, *180*, 3535–3544.

(38) Lin, J.; Su, Q.; Zhang, H.; Wang, S. Crystal Structure Dependence of the Luminescence of Rare Earth Ions (Ce^{3+}, Tb^{3+}, Sm^{3+}) in Y_2SiO_5. *Mate. Res. Bull.* **1996**, *31*, 189 – 196.

(39) Shannon, R. D. Revised Effective Ionic Radii and Systematic Studies of Interatomic Distances in Halides and Chalcogenides. *Acta Crystallogr. A* **1976**, *32*, 751–767.

(40) Swanson, D. K. and Peterson, R. C., Polyhedral Volume Calculations. *Can. Mineral.* **1980**, *18*, 153–156.

(41) Baur, W. H. The Geometry of Polyhedral Distortions. Predictive Relationships for the Phosphate Group. *Acta Crystallogr. B* **1974**, *30*, 1195–1215.

(42) Pauling, L. The Principles Determining the Structure of Complex Ionic Crystals. *J. Am. Chem. Soc.* **1929**, *51*, 1010–1026.

(43) Safarik, D.; Schwarz, R.; Hundley, M. Similarities in the C_p/T^3 Peaks in Amorphous and Crystalline Metals. *Phys. Rev. Lett.* **2006**, *96*, 195902(1–4).

(44) Melot, B.; Tackett, R.; O'Brien, J.; Hector, A.; Lawes, G.; Seshadri, R.; Ramirez, A. Large Low-Temperature Specific Heat in Pyrochlore $Bi_2Ti_2O_7$. *Phys. Rev. B* **2009**, *79*, 224111(1–5).

(45) Blackman, M. The Theory of the Specific Heat of Solids. *Rep. Prog. Phys.* **1941**, *8*, 11–30.

(46) Parkinson, D. H. The Specific Heats of Metals at Low Temperatures. *Rep. Prog. Phys.* **1958**, *21*, 226–270.

(47) Jeong, I.-K.; Heffner, R. H.; Graf, M. J.; Billinge, S. J. L. Lattice Dynamics and Correlated Atomic Motion from the Atomic Pair Distribution Function. *Phys. Rev. B* **2003**, *67*, 104301.

(48) Jeong, I.-K.; Proffen, T.; Mohiuddin-Jacobs, F.; Billinge, S. J. L. Measuring Correlated Atomic Motion Using X-ray Diffraction. *J. Phys. Chem. A* **1999**, *103*, 921–924.

(49) Proffen, T.; Page, K. L.; McLain, S. E.; Clausen, B.; Darling, T. W.; TenCate, J. A.; Lee, S.-Y.; Ustundag, E. Atomic Pair Distribution Function Analysis of Materials Containing Crystalline and Amorphous Phases. *Z. Kristallogr.* **2005**, *220*, 1002 .

Graphical TOC Entry